Grand Valley State University

ScholarWorks@GVSU

7-13-2011

Photodissociation of N₂O: Energy Partitioning

Johan A. Schmidt
University of Copenhagen, johanalbrechtschmidt@gmail.com

M. S. Johnson
University of Copenhagen

U. Lorenz
HASYLAB at DESY

George C. McBane
Grand Valley State University, mcbaneg@gvsu.edu

Reinhard Schinke
Max-Planck-Institut für Dynamik und Selbstorganisation, rschink@gwdg.de

Follow this and additional works at: https://scholarworks.gvsu.edu/chm_articles

 Part of the Biological and Chemical Physics Commons

Photodissociation of N$_2$O: Energy partitioning

J. A. Schmidt,[1,a)] M. S. Johnson,[1] U. Lorenz,[2] G. C. McBane,[3] and R. Schinke[4,b)]

[1]*Department of Chemistry, University of Copenhagen, Universitetsparken 5, DK-2100 Copenhagen Ø, Denmark*
[2]*HASYLAB at DESY, Notkestraße 85, D-22607 Hamburg, Germany*
[3]*Department of Chemistry, Grand Valley State University, Allendale, Michigan 49401, USA*
[4]*Max-Planck-Institut für Dynamik und Selbstorganisation, D-37073 Göttingen, Germany*

The energy partitioning in the UV photodissociation of N$_2$O is investigated by means of quantum mechanical wave packet and classical trajectory calculations using recently calculated potential energy surfaces. Vibrational excitation of N$_2$ is weak at the onset of the absorption spectrum, but becomes stronger with increasing photon energy. Since the NNO equilibrium angles in the ground and the excited state differ by about 70°, the molecule experiences an extraordinarily large torque during fragmentation producing N$_2$ in very high rotational states. The vibrational and rotational distributions obtained from the quantum mechanical and the classical calculations agree remarkably well. The shape of the rotational distributions is semi-quantitatively explained by a two-dimensional version of the reflection principle. The calculated rotational distribution for excitation with $\lambda = 204$ nm and the translational energy distribution for 193 nm agree well with experimental results, except for the tails of the experimental distributions corresponding to excitation of the highest rotational states. Inclusion of nonadiabatic transitions from the excited to the ground electronic state at relatively large N$_2$–O separations, studied by trajectory surface hopping, improves the agreement at high j. © *2011 American Institute of Physics*. [doi:10.1063/1.3602324]

I. INTRODUCTION

Nitrous oxide (N$_2$O) is a long-lived atmospheric trace gas ($\tau \sim 115$ a) mainly produced by nitrifying and denitrifying bacteria in the soil and the ocean; this source is enhanced by the use of fertilizer. Its mole fraction in the atmosphere has increased from a historic value of 255 ppb to 315 ppb today.[1,2] Nitrous oxide is a greenhouse gas with a global warming potential 300 times that of CO$_2$. Ninety percent is removed from the atmosphere by photolysis in the stratospheric UV window ($\sim 47\,500$ to $55\,000$ cm^{-1}), and ten percent by the reaction with O(^1D). This oxidation reaction produces nitric oxide radicals that deplete stratospheric ozone, and nitrous oxide has been identified as the main anthropogenic ozone depleting substance of the 21st century.[3] There are significant uncertainties in the sizes of atmospheric nitrous oxide sources, in part due to their diffuse nature.[1] Accurate determination of the photolysis sink is central to efforts to establish a budget for nitrous oxide using a mass balance approach.

The stratospheric absorption occurs on the red shoulder of the absorption maximum of the lowest absorption band (180 nm), which is due to excitation of the second $^1A'$ state,[4]

$$N_2O(X\ ^1A') + h\nu \rightarrow N_2O(2\ ^1A') \rightarrow N_2(X\ ^1\Sigma_g^+) + O(^1D)\,. \tag{1}$$
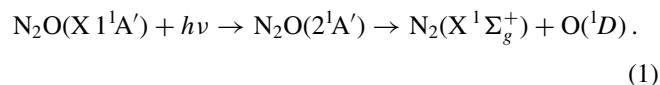
The absorption spectrum[5,6] has a broad Gaussian shape, reflecting a primarily direct fragmentation, with very weak vibrational structures due to temporary trapping of a tiny portion of the dissociating molecules near the Franck-Condon (FC) region.[7] Since the $1\ ^1A' \rightarrow 2\ ^1A'$ transition is dipole forbidden for linear N$_2$O, the transition dipole moment (TDM) is small for near-linear geometries and the absorption cross section is relatively small. The partitioning of the available energy into translational, vibrational, and rotational energy has been investigated in several laboratories using different methods.[8–14] The angular distribution of the products has also been studied intensively.[11,14]

A realistic description of the photofragmentation process requires accurate potential energy surfaces (PESs).[7] Two-dimensional PESs for several singlet and triplet states of linear N$_2$O were calculated by Hopper.[4] Brown *et al.*[15] and Daud *et al.*[16] constructed two-dimensional PESs for several low-lying singlet states. Because dissociation at 204 nm—at the onset of the absorption spectrum—showed very weak vibrational excitation of N$_2$,[9] the NN bond length, which changes by only 1% from N$_2$O to O + NN, was fixed at the X-state equilibrium value in these studies. PESs including all three internal degrees of freedom were calculated by Nanbu and Johnson[17] for the two lowest $^1A'$ states. The PESs of Brown *et al.*,[15] Daud *et al.*,[16] and Nanbu and Johnson[17] were used in wave packet calculations in order to unravel the dynamics of the UV dissociation of N$_2$O.[16–18] Although these calculations were helpful in understanding the main aspects of the fragmentation, the comparison with the experimental data was not convincing, and several facets remained unexplained, including the origin of the diffuse vibrational structures.

New PESs for the two lowest $^1A'$ states were recently calculated by Schinke and co-workers using a high level of electronic structure theory.[19,20] Although the electronic

a)Electronic mail: johanalbrechtschmidt@gmail.com.
b)Electronic mail: rschink@gwdg.de.

structure of N_2O near linearity is complex, the room-temperature absorption cross section calculated with only the $2\,^1A'$-state PES taken into account and nonadiabatic couplings to other states neglected agreed well with the measured cross section. In particular, it was shown that the weak vibrational structures reflect large-amplitude bending and NN stretching motion. The calculated temperature dependence of the absorption cross section[21] also agrees well with new high-precision measurements.[22]

In the present study, we investigate the energy partitioning among the three degrees of freedom of the products. We present both exact quantum mechanical wave packet calculations and classical trajectory calculations. The latter are useful in elucidating the dissociation dynamics.

II. CALCULATIONS

A. Potential energy surfaces

The PESs for the ground state (X) and the excited state (A), V_X and V_A, were calculated using the multi-configuration reference internally contracted configuration interaction (MRCI) theory[23,24] based on wave functions obtained by state-averaged full-valence complete active space self consistent field (CASSCF) calculations.[25,26] The augmented correlation consistent polarized valence quadruple zeta (aug-cc-pVQZ) basis set of Dunning[27] was employed. The Davidson correction was applied in order to approximately account for contributions of higher excitations and for size-extensive energies.[28] The corresponding TDM (μ_{XA}) was calculated at the same level of theory. All electronic structure calculations were performed with the MOLPRO suite of programs.[29] The PESs were calculated as functions of the Jacobi coordinates R (distance from O to the center of mass of NN), r (NN bond length), and γ (angle between **R** and **r**). Further details are given in Ref. 20. In what follows, all energies are normalized with respect to the equilibrium of the electronic ground state.

Figure 1 shows a two-dimensional cut of V_A for fixed bending angle $\gamma = 40°$. The solid dot marks the FC point, i.e., the maximum of $\sin\gamma\,\mu_{XA}^2\Psi_{(0,0,0)}^2$, where $\Psi_{(0,0,0)}$ is the ground-state vibrational wave function in the X state. The minimum energy path in the exit channel is slightly curved, i.e., the NN bond at the minimum changes from $2.24\,a_0$ at $R = 3.25\,a_0$ and $\gamma = 40°$ to $2.08\,a_0$ for the free nitrogen molecule. The PES has a bottleneck between $R = 3.5\,a_0$ and $4.0\,a_0$ through which the transient molecule must pass on its way to the product channel. This bottleneck is more pronounced for smaller angles. The NN bond weakens toward the $N(^2D) + NO(^2\Pi)$ dissociation limit at large r. More of this channel becomes accessible with increasing energy, with the result that the NN bond is significantly stretched and N_2 is highly vibrationally excited (see below). Moreover, a small part of the evolving wave packet is temporarily trapped and recurs in the Franck-Condon region. This recurrence is the origin of the diffuse vibrational structures of the absorption spectrum.[19,20]

The lower panel of Fig. 2 shows a two-dimensional cut of V_A for fixed $r = 2.20\,a_0$. The PES is symmetric with respect to $90°$ (provided the masses of the two N atoms are equal as assumed in this graph). The potential depends very strongly on the bending angle, and thus induces a large torque in the first moments of the bond breaking. The shallow minima around $50°$ and $130°$ become deeper, with respect to the asymptote, when the NN bond is stretched. These minima trap part of the wave packet for about one internal vibrational period of $\sim$75 fs, as described above.[19,20]

B. Quantum mechanical calculations

The quantum mechanical calculations were performed in the time domain by propagating a three-dimensional wave
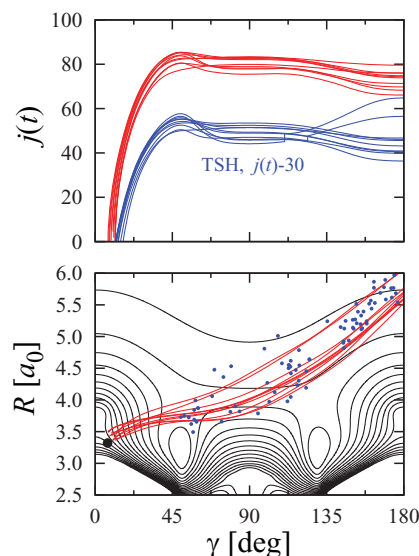
FIG. 2. Upper panel: Dependence of the classical rotational angular momentum of N_2, $j(R,r,\gamma|t)$, along the trajectories displayed in the lower part. The blue lines show $j(R,r,\gamma|t)$ as obtained from trajectory surface hopping (TSH) calculations, including nonadiabatic transitions between A and X (Sec. VI); for clarity, they are shifted downward by 30 units. Lower panel: Two-dimensional contour representation of the excited-state PES, V_A, for fixed $r = 2.20\,a_0$. The red lines show 10 randomly selected trajectories for a photolysis wavelength of 204 nm and the blue dots indicate the *first* hopping from A to X for a set of randomly selected surface hopping trajectories, also for 204 nm. See Fig. 1 for further details.

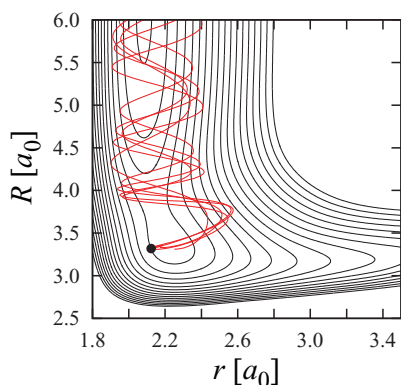

FIG. 1. Two-dimensional contour representation of the excited-state PES, V_A, for fixed $\gamma = 40°$. The highest contour is 8 eV and the contour spacing is 0.25 eV. The ● marks the FC point as defined in the text. The red lines show five randomly selected trajectories for a photolysis wavelength of 183 nm.

packet on the A-state PES.[7] The initial wave packet at $t = 0$, $\Phi(R, r, \gamma; 0)$, was chosen as the product of a vibrational wave function in the X state, $\Psi_{(v_1, v_2, v_3)}$, and the modulus of the TDM, μ_{XA}; version $\mu_{XA}^{(3)}$ described in Ref. 20 was used throughout the present study. The propagation was performed using the "symmetrical split operator algorithm."[30] Time steps of 0.1 fs were found to yield converged results. The propagation was terminated after 250 fs. The pseudospectral scheme presented by Le Quéré and Leforestier[31] was employed. In this scheme, the action of the radial part, i.e., R and r, of the kinetic energy operator on the wave packet is evaluated via the Fourier method,[32] while the angular part is evaluated by transforming between a grid representation and an associated Legendre polynomial basis set representation. The following grid parameters were employed: 400 and 80 equally spaced points in the intervals $2 a_0 \leq R \leq 13.97 a_0$ and $1.6 a_0 \leq r \leq 3.97 a_0$, respectively, and 256 angle grid points between $\gamma = 0$ and $\gamma = \pi$. To prevent reflections of the wave packet at the edges of the grid, absorbing boundaries were employed for $R > 10 a_0$ and $r > 3.5 a_0$.[33] All calculations were done for total angular momentum $J = 0$. The total absorption cross section $\sigma(E)$ was determined by Fourier transformation of the autocorrelation function.[7,34]

Final-state resolved partial cross sections $\sigma_{nj}(E)$ were obtained by the procedure of Balint-Kurti *et al.*[35] Time-dependent coefficients,

$$C_{nj}(t) = \int_0^\infty dr \int_0^\pi d\gamma \, \sin \gamma \left[\psi_{nj}(r) Y_j^m(\gamma) \right]^* \Phi(R_\infty, r, \gamma; t) \quad (2)$$

were calculated at a distance R_∞ far in the exit channel, where the interaction has decreased to zero. R_∞ was set to 9.98 a_0 in the present calculations. The ψ_{nj} and Y_j^m in Eq. (2) are the j-dependent vibrational and rotational wave functions of the free N₂ fragment, and m is either 0 or 1 (see below). The σ_{nj} were calculated by taking the half-Fourier transform of the coefficients $C_{nj}(t)$ (see Ref. 35 for further details). The quantum mechanical probabilities P_{nj} for a particular wavelength λ, which will be compared to the trajectory results and the experimental data, were obtained from the partial cross sections by integration over a narrow window $\lambda \pm 0.5$ nm.

Quantum calculations were performed for the initial states $(0, 0, 0)$, $(0, 1^1, 0)$, and $(0, 2, 0)$. The vibrational wave functions of the ground state were obtained by propagating a trial wave packet in imaginary time.[36] To obtain $(0, 2, 0)$ it was necessary to continuously project out the $(0, 0, 0)$ component of the trial wave packet. All calculations involving $(0, 0, 0)$ and $(0, 2, 0)$ were done using Legendre polynomials (i.e., $m = 0$), while the calculations for $(0, 1^1, 0)$ were done employing the associated Legendre polynomials with $m = 1$. All quantum mechanical calculations were performed with a modified version of the WAVEPACKET 4.6 program package.[37]

C. Classical trajectory calculations

The classical trajectory calculations were performed as described in Ref. 7. Initial coordinates R_0, r_0, and γ_0 and corresponding initial momenta P_0, p_0, and j_0 were randomly se-

lected in the six-dimensional phase space. Only phase space points with a specified total energy $E_{tot} \pm 0.010$ eV were accepted. Each trajectory was weighted by $w(R_0, r_0, \gamma_0) = \sin \gamma_0 \, \mu_{XA}^2 \Psi_{(0,0,0)}^2$ and a three-dimensional Gaussian function of the initial momenta. The exponential parameters of the latter were determined from the widths of $\Psi_{(0,0,0)}$ (cf. Chap. 5 of Ref. 7).

The final translational energy E_{trans} was directly evaluated from the momentum $P(t = \infty)$ at the end of the trajectory and the final rotational angular momentum quantum number j determined by binning of the (non-integer) $j(t = \infty)$. The vibrational quantum number n was determined by binning of the internal energy $E_{int} = E_{tot} - E_{trans}$ according to the rovibrational energies E_{nj} of the free N₂ for each value of j. The latter were calculated by solving the one-dimensional Schrödinger equation for the vibration of N₂ for $j = 0 - 100$. Two hundred thousand trajectories were typically calculated for each wavelength.

The vast majority of trajectories dissociate directly. Figure 1 shows several trajectories for photolysis at $\lambda = 183$ nm as functions of R and r. At the FC point $\partial V_A/\partial r$ is negative and therefore the NN bond is significantly stretched in the very first moments. As a consequence, the N₂ product is highly vibrationally excited. The degree of excitation depends on the photolysis wavelength in a systematic manner. The lower panel of Fig. 2 depicts randomly selected trajectories for 204 nm as functions of R and γ. The torque exerted on the N₂ fragment is exceedingly strong and this leads to extreme rotational excitation immediately after the release of the molecule in the excited state. Further details of the rotational excitation will be discussed in Secs. V and VI.

III. RESULTS

A. Vibrational distributions

Figure 3 shows rotationally summed partial cross sections σ_n for excitation from the $(0,0,0)$ state together with the total cross section σ vs. photon energy E_{ph}. The diffuse structures superimposed on the bell-shaped envelope of σ are also present in the partial cross sections, especially for the higher vibrational states. They are due to the temporary excitation of wide-amplitude bending and NN stretch motion and have been discussed in detail before.[19,20] The σ_n also have Gaussian-type envelopes with the maximum gradually shifting to higher E_{ph} with increasing n; the vibrational excitation therefore becomes stronger and stronger with increasing energy. The partial cross sections for initial states $(0, 1^1, 0)$ and $(0,2,0)$ are qualitatively similar. Examples of vibrational distributions P_n for three wavelengths are shown in Fig. 4. With decreasing λ the distributions become hotter and the maxima shift to higher n. The classical distributions are in remarkable agreement with the quantum mechanical results.

Partial cross sections and vibrational distributions like those in Figs. 3 and 4 are typical for dissociation processes when the FC point is displaced from the minimum (with respect to r) of the upper-state PES (cf. Chap. 9 of Ref. 7). This is the case for N₂O as illustrated in Fig. 1. With increasing energy the molecule starts to dissociate in the A state with a
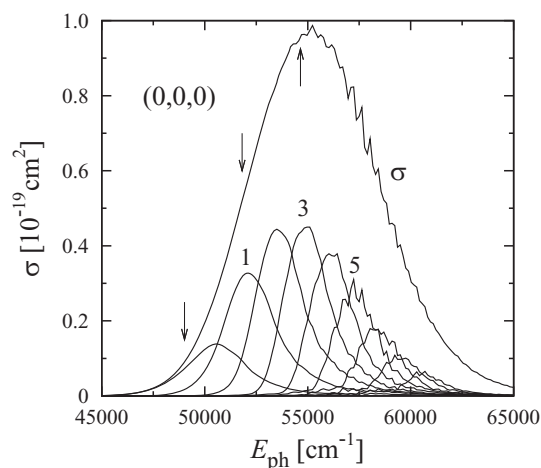
FIG. 3. Partial dissociation cross sections σ_n, summed over all final rotational states j vs. E_{ph}. The initial state is (0,0,0). The cross sections peak at successively higher energies with increasing n. The numbers indicate σ_1, σ_3, and σ_5, respectively. Also shown is the total absorption cross section σ. The arrows indicate the wavelengths for which vibrational and rotational distributions are presented: 204 nm, 193 nm, and 183 nm.

more and more compressed NN bond length which naturally leads to stronger vibrational excitation. A description of the UV dissociation of N_2O with a fixed NN bond length is therefore unrealistic.[16,38,39]
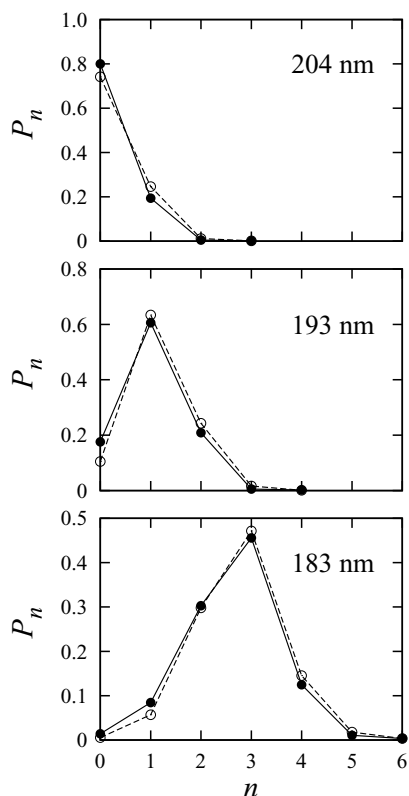

FIG. 4. Quantum mechanical (●) and classical (○) vibrational distributions P_n for three wavelengths as indicated. Both the quantum mechanical and the classical probabilities are normalized to unit sum.

B. Rotational distributions

The N_2 molecule is produced in extremely high rotational states. The reason is the very large torque $\partial V_A / \partial \gamma$ in the FC region (Fig. 2). Rotational distributions for different vibrational states and $\lambda = 204$ nm and 193 nm are shown in Figs. 5 and 6, respectively. All distributions are highly inverted and have an asymmetric bell shape with a rapid dropoff beyond the maximum. As is common in photodissociation,[7] the maximum shifts to lower j with increasing vibrational state, and to higher j with increasing photon energy. The quantum mechanical distributions show regular undulations on the low-j side of the maxima with amplitudes that depend on the vibrational state. These structures become more pronounced with increasing photon energy. They are independent of the numerical parameters of the calculations.

The classical rotational distributions are in very good agreement with the quantum mechanical ones, except for the oscillations, which are not reproduced. Note that there is no extra scaling factor for the various vibrational channels. The maxima of the classical distributions are consistently too high, by about two quanta; we do not consider this as a (numerical) coincidence, but as the result of a more basic effect (see below).

Calculations with an upper PES of the form[19] $\tilde{V}_A(R, r, \gamma) = V_A(R, r = 2.13, \gamma) + v_{NN}(r)$ yield much narrower rotational distributions. Here, $v_{NN}(r)$ is a harmonic potential with the force constant chosen so that the NN frequency in the X state is reproduced. The NN bond length is decoupled from R and γ in this potential, as it is in the calculations of Daud *et al.*[16] with fixed r. The distribution reported by Daud *et al.* for 203 nm peaks at $j = 74$, like the distribution in Fig. 5 for $n = 0$, but is also much narrower, with a
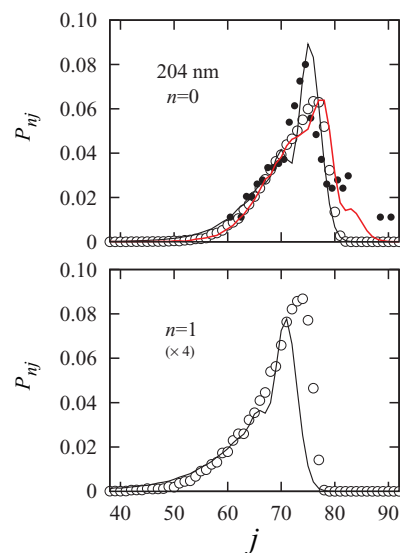

FIG. 5. Rotational state distributions P_{nj} for $\lambda = 204$ nm and $n = 0$ and 1. Comparison between quantum mechanical (solid lines) and classical (○) results. Both the quantum mechanical and the classical probabilities are normalized to unit sum. The ● represent the (averaged) experimental distributions of Kawamata *et al.* [Fig. 9(b) of Ref. 14]; they are arbitrarily scaled to the calculated distributions. Experimental data for $j = 83$ through 87 are not available. The red line shows the distribution obtained from the TSH calculations (Sec. VI). See the text for further details.
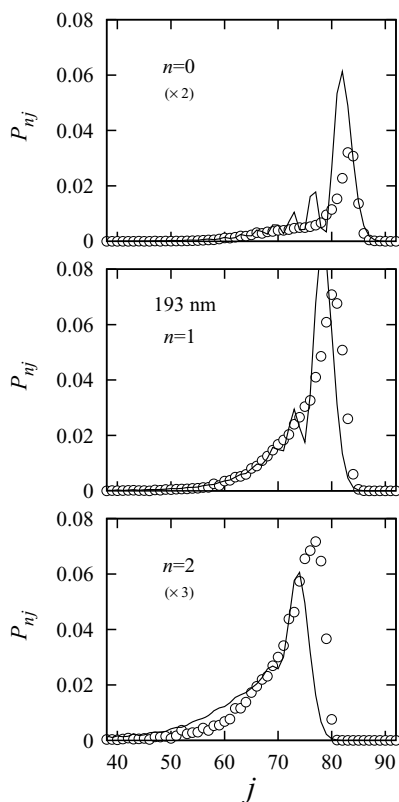
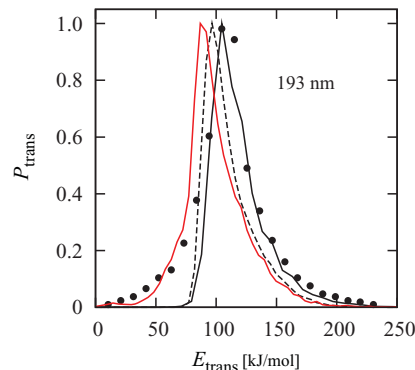FIG. 6. The same as in Fig. 5 for $\lambda = 193$ nm.

FIG. 7. Translational energy distributions for $\lambda = 193$ nm from quantum mechanical (black solid line) and classical (black dashed line) calculations. The ● represent experimental data from Fig. 3 of Ref. [8] and the red line shows the distribution obtained from TSH calculations (Sec. VI). The bin sizes are 4.8 and 8.4 kJ/mol in the classical and the quantum mechanical calculations, respectively. All distributions are normalized to one at the maximum. The (quantum mechanical) maximum available energy is 276 kJ/mol.

full width at half maximum of merely four rotational quanta. Vibrational motion along the dissociation path significantly broadens the rotational distributions.

The very steep decline of all rotational distributions beyond the maximum, the absence of the undulations in the classical calculations, and the consistent shift of the maxima of the classical distributions by ∼2 quanta to higher states as compared to the quantum results are indications that the distributions are governed by a rotational rainbow effect.[7,40,41] A qualitative analysis is given in Sec. V.

C. Translational energy distribution

Detailed rovibrational distributions of rotationally excited $N_2(^1\Sigma_g^+)$ apparently are difficult to measure. Information about the energy content of N_2 can be alternatively obtained from measurement of the velocities of the fragments by photofragment translational spectroscopy,[8] Doppler spectroscopy of $O(^1D)$,[10] or ion imaging.[42] Translational energy distributions P_{trans} have been measured for $\lambda = 204$ nm[42] and 193 nm.[8,10]

Figure 7 shows P_{trans} for 193 nm as obtained from the quantum mechanical and the classical calculations. In the quantum calculations, the translational energy for a state (n, j) is determined by $E_{trans} = E_{tot} - E_{nj}$. In the classical calculations, it is evaluated directly as $P^2(t \to \infty)/(2m)$, where m is the $N_2 + O$ reduced mass. As expected from the good agreement found for the state-resolved probabilities, the quantal and the classical translational distributions are almost identical. The narrowness reflects the remarkable "focusing"

of the trajectories (or wave packet): Because the A-state PES is strongly repulsive, the fragmentation is unusually direct and a small volume of the initial phase space is mapped onto a small volume of the final phase space.[7] The very steep decline of the low-E_{trans} branch mirrors the steep dropoff of all rotational distributions at their high-j end. The distributions for 204 nm are very similar; they peak at almost the same energy and are slightly broader.

IV. COMPARISON WITH EXPERIMENTAL RESULTS

Experimental information about the energy partitioning is available for two wavelengths, 204 nm and 193 nm. They are discussed separately.

A. 204 nm photolysis

Hanisco and Kummel[9] investigated the photodissociation of N_2O in the range 203–205 nm by state-resolved resonance enhanced multiphoton ionization (REMPI) in a one-color experiment. Similar experiments were reported by Neyer *et al.*[11] and Nishidi and Suzuki.[13] The maximum intensity was measured for $n = 0$ and $j = 74$ in all experiments. The spectra for $j \leq 74$ look regular and the determination of rotational state distributions is straightforward. They exhibit the expected 2:1 even-odd intensity ratio due to spin statistics; this effect is not taken into account in the calculations. All measured distributions start around $j \approx 55$ and reach half of the maximum value at ≈ 70. Beyond $j \approx 74$, the REMPI spectra are much less regular, probably as a result of perturbations in the N_2 a'' state,[9] and $n = 0$ and 1 transitions sometimes overlap. The high-j side of the $n = 0$ rotational distribution is therefore less well established.

We show the experimental distribution for $n = 0$ as read from Fig. 9(b) of Ref. [14] in Fig. 5. To suppress the even-odd oscillations, the probabilities for j and $j + 1$ were averaged and then plotted vs. $j + 1/2$. The agreement with the calculated distributions, especially the quantum mechanical one, is gratifying. The main discrepancy concerns the tail above

$j \sim 80$. While the measured distribution[11,14] extends to at least $j \sim 90$, both the quantum mechanical and the classical distributions are essentially zero above $j \approx 81$. The difference in terms of rotational quantum numbers may not appear very large. In terms of energy, however, it corresponds to 0.38 eV or 15% of the total available energy. This difference could be due to inaccuracy of the calculated PES, especially in its angle dependence. In Sec. VI, we will discuss another effect which may explain at least part of this discrepancy for the highest rotational states.

Kawamata *et al.*[14] reported rotational state distributions following photolysis of the initial states $(0,0,0)$, $(0, 1^1, 0)$, and $(0,2,0)$ with 204 nm light. The general shape does not change significantly; the peak shifts slightly from $j = 74$ for $(0,0,0)$ to 76–78 for $(0,2,0)$. The quantum mechanical calculations agree with this general behavior: The maximum shifts from 75 for $(0,0,0)$ to 77–78 for $(0,2,0)$.

Hanisco and Kummel[9] argued that the population of $n = 1$ is at most 2% of the $n = 0$ population. Subsequent investigations did not quote a particular value of the $n = 1$ population. Because of the overlapping transitions in the N_2 REMPI spectrum, Neyer *et al.*[11] "have not been able to make a quantitative measurement of the vibrational branching ratio." The calculations yield a 1:4 ratio for $\sigma(n = 1)/\sigma(n = 0)$ at 204 nm (Fig. 4). The vibrational distribution changes rapidly with photon energy and, in particular, the $\sigma(n = 1)/\sigma(n = 0)$ ratio rapidly increases at the onset of the absorption spectrum (Fig. 3). For example, at 210 nm the ratio is only 0.036 instead of 0.25 at 204 nm. Thus, small inaccuracies of the upper state PES, especially in the r coordinate, could easily explain the observed difference.

Employing two-dimensional ion imaging, Suzuki *et al.*[42] measured the translational energy distribution from 205 nm photolysis. P_{trans} has a symmetric bell shape with a maximum at 111 kJ/mol and is essentially zero beyond 210 kJ/mol. The computed distribution peaks near 105 kJ/mol and becomes zero around 202 kJ/mol. The calculated and the measured distributions differ, however, in their profiles. While the experimental P_{trans} is symmetric with respect to the maximum, the calculated one is asymmetric (similar to the distributions for 193 nm shown in Fig. 7) with a fast dropoff at the low-E_{trans} side.

B. 193 nm photolysis

Felder *et al.*[8] determined the photofragment translational energy distribution following photolysis at 193 nm by the time-of-flight method. Experimental data extracted from their Fig. 3 are shown in Fig. 7 in comparison to the calculated distributions. P_{trans} peaks at 106 kJ/mol and extends up to about 220 kJ/mol. Springsteen *et al.*[10] determined the translational energy distribution by measuring the Doppler profile of $O(^1D)$ with laser-induced fluorescence. The maximum occurs around 110 kJ/mol and the distribution has decreased to zero at 190 kJ/mol. The experimental P_{trans} agree well with each other,[10] except that a small shoulder at very low E_{trans} in the distribution of Felder *et al.*[8] is absent in the distribution of Ref. 10. The quantum mechanical and classical distributions reproduce the experiments satisfactorily. The main discrepancy is the lack of the low-energy tail below $\sim$75 kJ/mol, as was discussed for the 204 nm photolysis. A possible correction will be presented in Sec. VI.

V. TWO-DIMENSIONAL REFLECTION PRINCIPLE

Using classical and semiclassical arguments, we will explain—at a semi-quantitative level—the particular shapes of the rotational state distributions depicted in Figs. 5 and 6: the small widths, the asymmetric shape, the fast decline of the high-j branch, and the oscillations of the quantum mechanical distributions. To this end, we determined the classical vibrational and rotational excitation functions $N(r_0, \gamma_0)$ and $J(r_0, \gamma_0)$ by initiating trajectories on a two-dimensional grid (r_0, γ_0) near the FC region (cf. Chap. 5 of Ref. 7). The third initial coordinate, R_0, was chosen such that the trajectories had a particular total energy E_{tot}. Here, J is the (non-integer) final rotational quantum number at the end of the trajectory and N is the (non-integer) final vibrational quantum number.[43,44] All initial momenta were set to zero; this reduces the five-dimensional problem to two dimensions. Non-zero initial angular momenta j_0 have an especially large impact on $J(r_0, \gamma_0)$ and usually broaden the final rotational distributions.[45] However, including $j_0 \neq 0$ would drastically complicate the analysis without changing the general picture. Each initial point (r_0, γ_0) has an associated weight $w(r_0, \gamma_0)$ as defined in Sec. II C, which implicitly depends on E_{tot} and therefore on λ.

The excitation functions $J(r_0, \gamma_0)$ and $N(r_0, \gamma_0)$ for photolysis at 204 nm are depicted as two-dimensional contour representations in Fig. 8; the zigzag behavior of the contours in the middle-right part of the figure reflects the mesh of the grid. Because of the complexity of the A-state PES, especially for small angles, the topography of $J(r_0, \gamma_0)$ is intricate. Additionally, the PES is not monotonic along R for some regions of the (r_0, γ_0) grid, with the consequence that there may be more than one solution of $V(R_0, r_0, \gamma_0) = E_{\text{tot}}$ for a particular grid point. There are two maxima in $J(r_0, \gamma_0)$, a broad one near $(2.35\,a_0, 11°)$ and a narrow one near $(2.15\,a_0, 8°)$; a deep gap separates them. The weighting function $w(r_0, \gamma_0)$ is localized mainly on the slope of the broad maximum, slightly touching the bottom of the gap.

Within the semiclassical approach the probability for filling a rovibrational state (n, j) of N_2 is proportional to[7,43,44]

$$P_{\text{sc}}(n, j) \propto \left| \sum_\alpha p_{\text{cl}}^{1/2}(r_0^\alpha, \gamma_0^\alpha)\, e^{i\phi(r_0^\alpha, \gamma_0^\alpha)} \right|^2. \tag{3}$$

The function $\phi(r_0, \gamma_0)$ is a classical action integral along the trajectory. The summation runs over all trajectories with initial conditions $(r_0^\alpha, \gamma_0^\alpha)$ that simultaneously fulfill

$$N(r_0^\alpha, \gamma_0^\alpha) = n = 0, 1, \ldots, \tag{4}$$

$$J(r_0^\alpha, \gamma_0^\alpha) = j = 0, 1, \ldots, \tag{5}$$

where n and j are integer quantum numbers. The classical probabilities are defined by

$$p_{\text{cl}}(r_0^\alpha, \gamma_0^\alpha) = w(r_0^\alpha, \gamma_0^\alpha)\, D(r_0^\alpha, \gamma_0^\alpha)^{-1}, \tag{6}$$
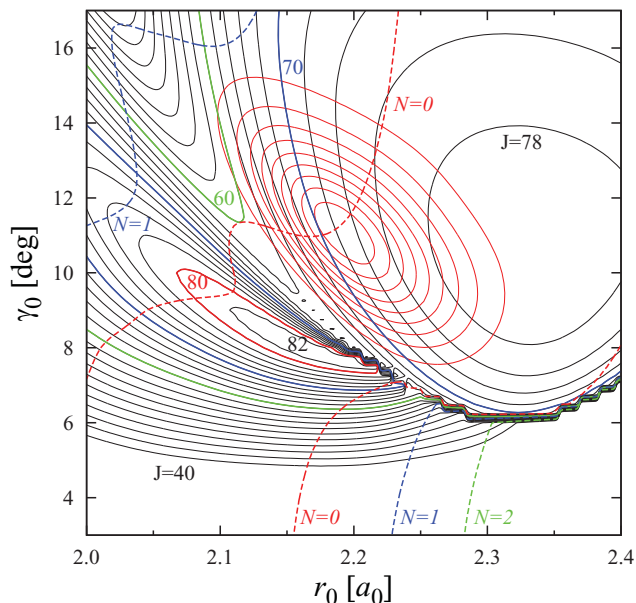
FIG. 8. Representation of the rotational excitation function $J(r_0, \gamma_0)$ (solid black contours) for $\lambda = 204$ nm. The lowest and highest contours are 40 and 82, respectively, and the spacing is $\Delta J = 2$. For guidance, the contours for $J = 60$, 70, and 80 are colored. The colored broken contours represent the vibrational excitation function $N(r_0, \gamma_0)$ for $N = 0$ (red), 1 (blue), and 2 (green). Also shown are contours (closed solid red lines in the center) of the weighting function $w(r_0, \gamma_0)$; the lowest (highest) contour represents 10% (90%) of the maximum value.

where D is the Jacobi determinant

$$D = \begin{vmatrix} \dfrac{\partial J}{\partial r_0} & \dfrac{\partial J}{\partial \gamma_0} \\[2mm] \dfrac{\partial N}{\partial r_0} & \dfrac{\partial N}{\partial \gamma_0} \end{vmatrix}, \tag{7}$$

evaluated at $(r_0^\alpha, \gamma_0^\alpha)$. D becomes important near a maximum in $J(r_0, \gamma_0)$ or $N(r_0, \gamma_0)$, because then the determinant vanishes and p_{cl} diverges, producing a rainbow effect.[7,43,44,46] Similar enhancements in the final population of a particular final state will also occur if the $J(r_0, \gamma_0)$ and $N(r_0, \gamma_0)$ curves corresponding to that state are tangent at a point or nearly coincident over an extended region. In that case the gradients of the N and J functions will be parallel, and D will again vanish. It is difficult to find all the trajectories that are necessary to use Eqs. (3)–(7) for a quantitative application. Moreover, a "uniform" semiclassical formulation (using Airy functions) is, in general, more appropriate for a quantitative treatment than the "primitive" semiclassical expression Eq. (3). Nevertheless, Eqs. (3)–(7) are useful for qualitative interpretation of the quantum mechanical and classical results.

The population of a particular N₂ state is classically allowed if the set of Eqs. (4) and (5) has at least one real solution. If there are only complex solutions—after analytical continuation of $J(r_0, \gamma_0)$ and $N(r_0, \gamma_0)$ into the complex plane[43,44]—the transition is classically forbidden and the probability decays exponentially with increasing departure from the real (r_0, γ_0) plane. If there is one and only one solution $(r_0^\alpha, \gamma_0^\alpha)$, the phase term is irrelevant and the semiclassical probability equals the classical one. The existence of more than one solution can lead to interference oscillations governed by the different phases $\phi(r_0, \gamma_0)$ for each of the con-

tributing trajectories. The amplitudes of the oscillations are related to the ratios of the corresponding $p_{cl}^{1/2}$.

The rotational distribution for $n = 0$ in Fig. 5 is determined by the crossings of the $N(r_0, \gamma_0) = 0$ contours in Fig. 8 with the contours of $J(r_0, \gamma_0)$ for integer values. In other words, $P_{n=0,j}$ basically reflects $w(r_0, \gamma_0)$ along the $N = 0$ contour; this is an example of the reflection principle described in Chap. 6 of Ref. 7. The section of the contour that runs more or less parallel to the r_0-axis ($r_0 = 2.1\, a_0$ − 2.2 a_0) governs the low-j part from $j \approx 60$ to the maximum of w around $j = 72 - 73$. $J(r_0, \gamma_0)$ rises steeply along this branch and therefore the low-j part of $P_{n=0,j}$ is comparatively broad. The branch of $N(r_0, \gamma_0) = 0$ running approximately parallel to the γ_0-axis ($\gamma_0 = 12° - 16°$), on the other hand, determines the high-j part of the distribution. $J(r_0, \gamma_0)$ is flat along this branch with a maximum near $J = 76$. Since the weighting function w is already very small at this crossing, no strong maximum due to the nearly coincident $J = 76$ and $N = 0$ curves is discernible in the classical distribution. Beyond $j \sim 76$, Eqs. (4) and (5) have only complex solutions and therefore the probability drops to zero very rapidly. The distribution obtained from simplified calculations with all initial momenta set to zero, like those used to construct Fig. 8, has its maximum at 74–75 and is negligible at $j \sim 80$. The maximum of $P_{n=0,j}$ and its shape is thus determined by the interplay of w and D^{-1} along the $N(r_0, \gamma_0) = 0$ contour as well as the exponential decay into the classically forbidden region.

So far, we have mainly considered the upper $N(r_0, \gamma_0) = 0$ contour in Fig. 8, and particularly the short segment cutting through the broad maximum of $J(r_0, \gamma_0)$, because it dominates the rotational distribution. However, the segment at $r_0 \approx 2.1\, a_0$ and $\gamma_0 \approx 10.5°$ of the same contour also yields contributions to the sum in Eq. (3) and so does the other $N(r_0, \gamma_0) = 0$ contour in the lower right corner. These additional phase space points can interfere with the main trajectory discussed in the previous paragraph and therefore might cause interference structures. Because the weights for these other trajectories are comparatively small, the corresponding oscillations in $P_{n=0,j}$ are expected to have low intensities. Indeed, the quantum mechanical probability in the upper panel of Fig. 5 shows two low-intensity maxima at $j \approx 65$ and 70.

The two $N(r_0, \gamma_0) = 1$ contours are well outside the region where the absorption predominantly takes place and therefore the probability for $n = 1$ is very small. In the simplified calculations it is just 5%. The same arguments as for $n = 0$ rationalize the observation that the rotational distribution for $n = 1$ rises slowly on the low-j side, reaches a rainbow-type maximum around 68, and then rapidly decreases to zero. The calculations with zero initial momenta yield a maximum at 68 and zero probability above $j = 73$. The tiny oscillation in the quantal probability may be due to the interference between trajectories belonging to the two $N(r_0, \gamma_0) = 1$ branches.

Figure 9 shows the vibrational and rotational excitation functions for $\lambda = 193$ nm. The general appearance is similar to the results for 204 nm. The maximum of $w(r_0, \gamma_0)$ has shifted from $\gamma_0 = 11°$ to about 8°. The broad maximum of $J(r_0, \gamma_0)$ has been moved to the lower right corner of the
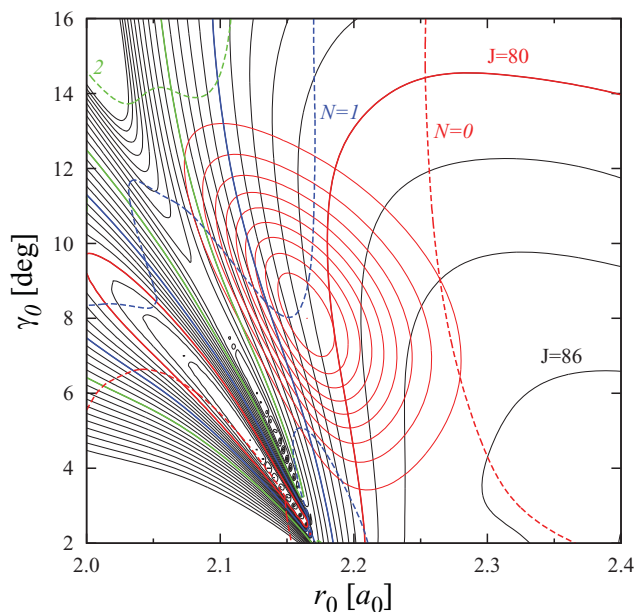
FIG. 9. The same as in Fig. 8 for $\lambda = 193$ nm.

figure and the narrow maximum ($J \sim 86$) is located around ($2.1\,a_0$, $5°$). The qualitative explanation of the vibrational and rotational state distributions follows exactly the discussion for 204 nm. For example, Fig. 9 readily predicts that $P_{n=0}$ and $P_{n=2}$ are small; the simplified calculations yield 9% and 6%, respectively. The rotational distributions for $n = 0 - 2$ are expected to peak around $j = 85$, 80, and 72 and the calculations confirm this. For $n = 1$ and j around 70 there are clearly two real-valued contributions to the semiclassical probability, originating from the two different branches of $N(r_0, \gamma_0) = 1$, one in the upper part and one in the lower part of the figure. The corresponding weights are not too different so that the resulting interference oscillations should be clearly discernible. The quantum mechanical probability $P_{n=1,j}$ in Fig. 6 confirms this semiclassical prediction.

Analysis of the classical excitation functions demonstrates that the dissociation of N_2O on the $2^1A'$ PES is a complicated process involving all internal degrees of freedom. The rotational distribution for a particular vibrational state is governed by a small region of the initial phase space. Both the reflection of the weighting function and a rainbow effect due to the shapes of the excitation functions determine the shape of $P_{n,j}$. Interference oscillations are common features. They are more pronounced for shorter wavelengths; however, the corresponding initial phase space structure is much more complicated and therefore not discussed here.

VI. NONADIABATIC A→X TRANSITIONS

The calculated rotational distribution for excitation with $\lambda = 204$ nm does not reproduce the tail to very high states up to $j \sim 90$ as observed experimentally (Fig. 5). Similarly, the calculations do not yield the tail to very low energies of the measured E_{trans} distribution for 193 nm (Fig. 7). Both imperfections have the same origin, namely, the rather sharp cut-off of the final rotational angular momentum at a particular

wavelength-dependent limit as shown by Figs. 8 and 9. The evolution of the classical $j(t)$ along the trajectories elucidates the dynamical constraints leading to the limitation of the final j; this is illustrated in the upper panel of Fig. 2. The N_2 entity is strongly excited by the torque $\partial V_A/\partial \gamma$ in the first moments of the fragmentation. The torque first becomes zero around $\gamma \sim 45°$ and then changes its sign with the result that the rotation is decelerated by a few quanta. The rotation slows down again when the trajectory hits the repulsive branch of V_A at the other end of the NN rotor around $180°$. Thereafter, $j(t)$ remains constant.

Small changes of the angle dependence of V_A are imaginable that could change the exit channel dynamics in such a way that states beyond $j \approx 80$ become populated. There is, however, another effect which may influence the course of the trajectories and thus the final distributions. The saddle of the A-state PES around $50°$ and $R = 3.75\,a_0$ is caused by an avoided crossing with the X state,[17,20] as illustrated in the upper panel of Fig. 10, which shows $V_A - V_X$. In this region the molecule can undergo a transition from A to X, because the energy separation is relatively small. Both states belong to the same symmetry group and since they approach the same dissociation limit, $V_A - V_X$ eventually goes to zero as R increases and transitions between X and A are inherent. If the transition to the X state occurs sufficiently early along the trajectory, the coordinate dependence of V_X—which is different from that of V_A—can affect the final rotational state distribution of $N_2(X)$. Whether $j(t)$ decreases or increases before it eventually becomes constant depends on the sign and magnitude of $\partial V_{A(X)}/\partial \gamma$. For carbonyl sulfide (OCS) the impact of nonadiabatic transitions to the ground state during fragmentation has been investigated by Suzuki *et al.*[47]

We tested the influence of the nonadiabatic transitions by means of trajectory surface hopping (TSH) calculations using the method of Tully:[48] The time-dependent Schrödinger
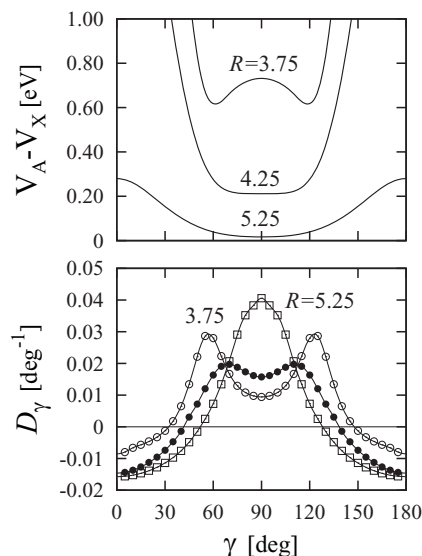

FIG. 10. Upper panel: Energy separation $V_A - V_X$ vs. γ for fixed R as indicated and $r = 2.13\,a_0$. Lower panel: Kinetic coupling element D_γ vs. γ for $R = 3.75\,a_0$ (○), $4.25\,a_0$ (●), and $5.25\,a_0$ (□) and $r = 2.13\,a_0$. The symbols represent the calculated data points.

equation for the electronic state amplitudes $a_k(t)$ ($k =$ A or X) is solved along each classical trajectory, and according to a specific criterion the molecule is allowed to hop from one state to the other. The momenta in the new state are adjusted after each transition to satisfy energy conservation. Details of the implementation in our classical trajectory code are given in Ref. 49.

In the current study the electronic Schrödinger equation was solved in the adiabatic representation. The coupling between the states was therefore given by

$$\chi = \dot{R} D_R + \dot{r} D_r + \dot{\gamma} D_\gamma , \qquad (8)$$

where $D_\xi = \langle \Xi_X | \partial / \partial \xi | \Xi_A \rangle$ ($\xi = R$, r, and γ) are the nonadiabatic kinetic coupling terms with Ξ_X and Ξ_A being the (nuclear-coordinate dependent) adiabatic electronic wave functions in X and A, respectively. The dots in Eq. (8) represent differentiation with respect to t.

The kinetic coupling terms were calculated using the MOLPRO suite of programs[29] at the CASSCF level of theory and employing the aug-cc-pVTZ basis set.[27] Calculations at the MRCI level or using a larger basis set yielded very similar results. Because the angular motion is the most important, we considered only the last term in Eq. (8). The lower panel of Fig. 10 shows D_γ for several values of R and $r = 2.13 \, a_0$. D_γ is symmetric with respect to $\gamma = 0$ and $90°$. For smaller values of R, it peaks near $60°$ and $120°$, where the X and the A state have avoided crossings. With increasing R, however, the peaks move closer to $90°$ where the energy separation is smallest. The coupling element does not necessarily go to zero for linear N₂O although $V_A - V_X$ is large. D_γ is a function of all coordinates. It was calculated on an appropriate three-dimensional grid and interpolated by cubic splines for use in the TSH calculations.

The points where the first hopping from V_A to V_X occurred are indicated in the lower panel of Fig. 2 for a randomly chosen batch of trajectories. Transitions begin when the region of the avoided crossing is reached, that is, when the energy separation is sufficiently small. As the fragmentation continues, the molecule can make further jumps between the X and the A state. Since the energy separation diminishes while the coupling element remains finite, it becomes meaningless to assign the system to either of the states when $R \to \infty$. The averaged probabilities for being in X or A at the end of the trajectories are about 50%. However, only the transitions taking place before $R \approx 5.5 \, a_0$ are important for the energy partitioning; both PESs are more or less isotropic for larger N₂–O separations and $j(t)$ becomes constant. The upper panel of Fig. 2 shows j vs. γ for 10 randomly selected trajectories obtained with the TSH program. At least two of them behave differently from those calculated without transitions: They clearly illustrate the surmised increase of j after $\gamma \approx 90°$. The small discontinuities are due to the adjustment of the momenta to enforce energy conservation.

TSH calculations were carried out for 204 nm and 193 nm photolysis. The rotational distribution for 204 nm and $n = 0$ is shown in Fig. 5 in comparison to the results of the single-state calculations and the experimental distribution. It has been slightly rescaled to roughly match the single-state classical distribution at the maximum. The influence of nona-

diabatic transitions is clearly visible in the form of a tail extending up to $j = 90$. Taking the (assumed) uncertainty of the experimental data into consideration, the agreement with the data of Kawamata et al.[14] is satisfactory. Similar improvement is observed for the 193 nm E_{trans} distribution in Fig. 7. The possibility of continuing the dissociation on the X-state PES shifts the maximum to slightly lower energies and yields the tail extending down to 25 kJ/mol, which is missing in the one-state treatment. A tiny shift to higher E_{trans} would lead to perfect agreement with the experimental data of Felder et al.[8]

VII. CONCLUSIONS

The photodissociation of N₂O in the first absorption band is a very fast process with strong internal energy redistribution along the fragmentaton path. The degree of vibrational excitation of $N_2(^1\Sigma_g^+)$ is small at the onset of the absorption band but it gradually increases with photon energy. The vibrational distributions are generally narrow with the maximum shifting to higher and higher states. N₂ is created with an unusually high degree of rotational excitation caused by the strong torque on the upper state potential energy surface. The rotational distributions are highly inverted and narrow: A small volume of the initial phase space is mapped onto a small volume of the final momentum space. The overall shape of the rotational distributions is explained by a two-dimensional reflection principle. The fast dropoff on the high-j side of the pronounced maximum is partly caused by a rotational rainbow effect. Nonadiabatic transitions from the upper to the lower state at relatively large separations, studied by the trajectory surface hopping method, cannot be neglected. They extend the rotational distributions to even higher states, which are dynamically inaccessible if dissociation on only the excited state is taken into account.

Classical trajectory calculations are in very good agreement with the results of exact quantum mechanical calculations, as expected for a fast and direct dissociation with high excess energy. The calculated results agree well with the available experimental data. In view of the good description of the absorption spectrum, including its temperature dependence and diffuse vibrational structures, the product vibrational and rotational distributions, and the effect of isotopic substitution on the absorption cross section,[50] we conclude that the photodissociation of nitrous oxide in the UV wavelength region is basically understood.

[1]P. R.V. Forster, P. Artaxo, T. Berntsen, R. Betts, D. W. Fahey, J. Haywood, J. Lean, D. C. Lowe, G. Myhre, J. Nganga, R. Prinn, G. Raga, M. Schulz, and R. Van Dorland, in *Climate Change 2007: The Physical Science Basis. Contribution of Working Group I to the Fourth Assessment Report of the Intergovernmental Panel on Climate Change*, edited by S. Solomon, D. Quin, M. Manning, Z. Chen, M. Marquis, K. B. Averyt, M. Tignor, and H. L. Miller (Cambridge University Press, Cambridge/New York, 2007).
[2]WMO Scientific Assessment of Ozone Depletion: 2006, Global Ozone Research and Monitoring Project, Report No. 50, World Meteorological Organization, 2007.

[3] A. R. Ravishankara, J. S. Daniel, and R. W. Portmann, Science **326**, 123 (2009).

[4] D. G. Hopper, J. Chem. Phys. **80**, 4290 (1984).

[5] G. S. Selwyn and H. S. Johnston, J. Chem. Phys. **74**, 3791 (1981).

[6] K. Yoshino, D. E. Freeman, and W. H. Parkinson, Planet. Space Sci. **32**, 1219 (1984).

[7] R. Schinke, *Photodissociation Dynamics* (Cambridge University Press, Cambridge, England, 1993).

[8] P. Felder, B.-M. Haas, and J. R. Huber, Chem. Phys. Lett. **186**, 177 (1991).

[9] T. F. Hanisco and A. C. Kummel, J. Phys. Chem. **97**, 7242 (1993).

[10] L. L. Springsteen, S. Satyapal, Y. Matsumi, and P. L. Houston, J. Phys. Chem. **97**, 7239 (1993).

[11] D. W. Neyer, A. J. R. Heck, and D. W. Chandler, J. Chem. Phys. **110**, 3411 (1999).

[12] A. M. Rijs, E. H.G. Backus, C. A. de Lange, M. H. M. Janssen, K. Wang, and V. McKoy, J. Chem. Phys. **114**, 9413 (2001).

[13] T. Nishide and T. Suzuki, J. Phys. Chem. A **108**, 7863 (2004).

[14] H. Kawamata, H. Kohguchi, T. Nishide, and T. Suzuki, J. Chem. Phys. **125**, 133312 (2006).

[15] A. Brown, P. Jimeno, and G. G. Balint-Kurti, J. Phys. Chem. A **103**, 11089 (1999).

[16] M. N. Daud, G. G. Balint-Kurti, and A. Brown, J. Chem. Phys. **122**, 054305 (2005).

[17] S. Nanbu and M. S. Johnson, J. Phys. Chem. A **108**, 8905 (2004).

[18] M. S. Johnson, G. D. Billing, A. Gruodis, and M. H. M. Janssen, J. Phys. Chem. A **105**, 8672 (2001).

[19] R. Schinke, J. Suarez, and S. C. Farantos, J. Chem. Phys. **133**, 091103 (2010).

[20] R. Schinke, J. Chem. Phys. **134**, 064313 (2011).

[21] R. Schinke, "Photodissociation of N_2O: Temperature dependence" Chem. Phys. (submitted).

[22] N. Rontu Carlon, D. K. Papanastasiou, E. L. Fleming, C. H. Jackman, P. A. Newman, and J. B. Burkholder, Atmos. Chem. Phys. **10**, 6137 (2010).

[23] H.-J. Werner and P. J. Knowles, J. Chem. Phys. **89**, 5803 (1988).

[24] P. J. Knowles and H.-J. Werner, Chem. Phys. Lett. **145**, 514 (1988).

[25] H.-J. Werner and P. J. Knowles, J. Chem. Phys. **82**, 5053 (1985).

[26] P. J. Knowles and H.-J. Werner, Chem. Phys. Lett. **115**, 259 (1985).

[27] T. H. Dunning, Jr., J. Chem. Phys. **90**, 1007 (1989).

[28] S. R. Langhoff and E. R. Davidson, Int. J. Quantum Chem. **8**, 61 (1974).

[29] MOLPRO, a package of *ab initio* programs designed by H.-J. Werner and P. J. Knowles, version 2006, R. Lindh, F. R. Manby, M. Schütz *et al.* Also see http://www.molpro.net.

[30] M. D. Feit, J. A. Fleck, and A. Steiger, J. Comput. Phys. **47**, 412 (1982).

[31] F. Le Quéré and C. Leforestier, J. Chem. Phys. **92**, 247 (1990).

[32] D. Kosloff and R. Kosloff, J. Comput Phys. **52**, 35 (1983).

[33] R. Kosloff and D. Kosloff, J. Comput. Phys. **63**, 363 (1986).

[34] G. G. Balint-Kurti, Adv. Chem. Phys. **128**, 249 (2004).

[35] G. G. Balint-Kurti, R. N. Dixon, and C. C. Marston, J. Chem. Soc., Faraday Trans. **86**, 1741 (1990).

[36] R. Kosloff and H. Tal-Ezer, Chem. Phys. Lett. **127**, 223 (1986).

[37] B. Schmidt and U. Lorenz, WAVEPACKET 4.6, a program package for quantum-mechanical wavepacket propagation and time-dependent spectroscopy (2009). Also see http://wavepacket.sourceforge.net.

[38] M. N. Daud and G. G. Balint-Kurti, Chin. Phys. Lett. **26**, 073302 (2009).

[39] G. G. Balint-Kurti, Theor. Chem. Acc. **127**, 1 (2010).

[40] R. Schinke, J. Phys. Chem. **90**, 1742 (1986).

[41] R. Schinke, J. Chem. Phys. **85**, 5049 (1986).

[42] T. Suzuki, H. Katayanagi, Y. Mo, and K. Tonokura, Chem. Phys. Lett. **256**, 90 (1996).

[43] W. H. Miller, Adv. Chem. Phys. **25**, 69 (1974).

[44] W. H. Miller, Adv. Chem. Phys. **30**, 77 (1975).

[45] R. Schinke, J. Phys. Chem. **92**, 3195 (1988).

[46] R. Schinke and J. M. Bowman, in *Molecular Collision Dynamics*, edited by J. M. Bowman (Springer-Verlag, Heidelberg, 1983).

[47] T. Suzuki, H. Katayanagi, S. Nanbu, and M. Aoyagi, J. Chem. Phys. **109**, 5778 (1998).

[48] J. C. Tully, J. Chem. Phys. **93**, 1061 (1990).

[49] R. Schinke and G. C. McBane, J. Chem. Phys. **132**, 044305 (2010).

[50] J. A. Schmidt, M. S. Johnson, and R. Schinke, Atmos. Chem. Phys. Discuss. **11**, 16075 (2011).